

The Catalytic Mechanism of the Plastic-Degrading Enzyme Urethanase UMG-SP2

Paiva, P.^[1], Teixeira, L.M.C.^[1], Wei, R.^[2], Liu, W.^[3], Morth, J.P.^[4], Westh, P.^[4], Petersen, A.R.^[5], Johansen, M.B.^[5], Sommerfeldt, A.^[5], Sandahl, A.^[5], Otzen, D. E.^[6], Fernandes, P.A.^[1], and Ramos, M.J.^[1]*

^[1] LAQV@REQUIMTE, Departamento de Química e Bioquímica, Faculdade de Ciências, Universidade do Porto, Rua do Campo Alegre s/n, 4169-007, Porto, Portugal.

^[2] Department of Biotechnology & Enzyme Catalysis, Institute of Biochemistry, University of Greifswald, Felix-Hausdorff-Str. 4, 17487 Greifswald, Germany.

^[3] University of Chinese Academy of Sciences, 19A Yuquan Road, Beijing 100049 China.

^[4] Department of Biotechnology and Biomedicine, Technical University of Denmark, Søtofts Plads, DK-2800, Kongens Lyngby, Denmark.

^[5] Teknologisk Institut, DK-8000, Kongsvang Alle 29, Aarhus, Denmark

^[6] Interdisciplinary Nanoscience Center (iNANO). Aarhus University, Gustav Wieds Vej 14, DK - 8000 Aarhus, Denmark

*email: mjramos@fc.up.pt

ABSTRACT:

The recently discovered metagenomic urethanases UMG-SP1, UMG-SP2, and UMG-SP3 have emerged as promising tools to improve existing chemical processes for polyurethane (PU) waste recycling. These enzymes are capable of breaking down urethane bonds in low molecular weight dicarbamates using the Ser-Ser_{cis}-Lys triad for catalysis, similar to other members of the amidase signature protein superfamily. Understanding the catalytic mechanism of these urethanases is crucial for enhancing their enzymatic activity and improving PU bio-recycling processes. In this study, we employed hybrid quantum mechanics/molecular mechanics methods to delve into the catalytic machinery of the UMG-SP2 urethanase in breaking down a model PU substrate. Our results indicate that the reaction proceeds in two stages: STAGE 1 - acylation, in which the enzyme becomes covalently bound to the PU substrate, releasing an alcohol-leaving group; STAGE 2 - deacylation, in which a catalytic water hydrolyzes the enzyme:ligand covalent adduct, releasing the product in the form of a highly unstable carbamic acid, expected to rapidly decompose into an amine and carbon dioxide. We found that STAGE 1 comprises the rate-limiting step of the overall reaction, consisting of the cleavage of the substrate's urethane bond by its ester moiety and the release of the alcohol-leaving group (overall Gibbs activation energy of 20.8 kcal·mol⁻¹). Lastly, we identified point mutations that are expected to enhance the enzyme's turnover for the hydrolysis of urethane bonds by stabilizing the macrodipole of the rate-limiting transition state. These findings expand our current knowledge of urethanases and homolog enzymes from the amidase signature superfamily, paving the way for future research on the enzymatic depolymerization of PU plastic materials.

Keywords: *Thermoset polyurethane, urethanase, enzyme mechanism, molecular dynamics, QM/MM.*

Introduction

Plastics have become fundamental to modern society, due to their durability, versatility, and low production cost. This reliance on plastics is observed in almost every economic or industrial sector, *e.g.*, packaging, construction, electronics, and many more,¹ including in many polymer innovations. Consequently, global plastic production has significantly increased over the past 50 years. A combination of widespread use and poor end-of-life planning have led to the accumulation of these recalcitrant materials throughout the environment.² In 2022, < 10% of all globally produced plastic was recycled.³ This buildup now poses serious threats to both the environment and human health.⁴ Therefore, there is an urgent need for the development of efficient, sustainable, and economically viable solutions to address the end-of-life of these materials.

Polyurethanes (PU) are among the most widely used types of recalcitrant plastics, due to their versatility. Of the 400 million tons of plastic produced globally on an annual basis, 5.3% are PU, ranking it the 6th most produced synthetic polymer.³ The urethane bond, a traditional name for the carbamate bond, $R_1OC=OCNR_2R_3$, is formed by combining an isocyanate (typically methylene diphenyl diisocyanate or toluene diisocyanate) with a polyol (*e.g.*, polyethers and polyesters). Depending on the formulation, polyurethane materials can be either thermoplastic or thermoset polymers, allowing for a wide range of applications, including adhesives, coatings, foams, elastomers, and sealants.⁵

Unlike thermoplastics, thermoset PUs are insoluble and highly cross-linked structures. They cannot be reshaped by heat, as they decompose at high temperatures.⁶ Consequently, recycling PUs is limited to grinding, adhesive bonding, or chemical methods such as glycolysis. The first two are secondary recycling processes, which repurpose the recycled polymer for less demanding applications, while the third option is a tertiary recycling method that uses the waste polymers as feedstock to produce other chemicals.⁷ The current options for thermoset PU recycling are far from satisfactory, as either the recycled polymers suffer a considerable decrease in performance, significantly reducing their market value, or the recycling process consumes high amounts of energy (*ca.* 817 kg CO₂-eq./t PU waste).⁸ In 2018, hard and flexible foams constituted 68% of the PU market share, indicating that most of the applications used thermoset PU.⁹ Therefore, developing a more efficient and environmentally friendly recycling method is also economically beneficial.

Enzymatic depolymerization is one of the most promising strategies for addressing the end-of-life of recalcitrant plastics. Unlike chemical recycling, this efficient soft process does not require harsh conditions (*e.g.*, high temperatures and/or of toxic compounds).¹⁰ Since Yoshida *et al.*¹¹ discovered the first PETase, an enzyme capable of degrading polyethylene terephthalate (PET), there has been a rise in interest in the enzymatic depolymerization of PET.¹²⁻¹⁴ Building on this, the company Carbios engineered an enzyme that hydrolyzes around 90% of a PET plastic bottle within 10 hours, demonstrating the potential of enzymatic depolymerization.¹⁵ Carbios has now implemented enzymatic depolymerization of PET on an industrial scale. Considering the structural similarities between PET and PUs, this proven strategy can also potentially be applied to depolymerize thermoset PUs.

In 2023, Branson *et al.*¹⁶ discovered three urethanase enzymes (UMG-SP1, UMG-SP2, and UMG-SP3) capable of hydrolyzing the urethane bond. These enzymes were identified through a metagenome screening from an isolated soil sample DNA exposed to PU. All three enzymes hydrolyzed a broad range of low molecular weight dicarbamates (PU mimics). Interestingly, UMG-SP2 hydrolyzed 90% of one of these substrates within 24 h. Branson *et al.*¹⁶ hypothesized that urethanases could be used in a chemoenzymatic process to recycle PUs. This approach involved subjecting post-consumer PU material to a chemical recycling method, generating low molecular weight dicarbamates and polyols. Unlike polyols, dicarbamates require harsh conditions and high energy costs for recycling. Therefore, the authors suggested using urethanases to hydrolyze these compounds. As proof of concept, they subjected a PU foam, obtained from a post-consumer pillow, to their envisioned chemoenzymatic process. First, the foam was subjected to alcoholysis with diethylene glycol, converting the PU into dicarbamates and polyol. Subsequently, these dicarbamates were incubated with UMG-SP2, leading to complete hydrolysis of all dicarbamates within 48 h at sufficiently high enzyme concentrations. These results showcased the ability of UMG-SP2 to degrade the urethane bond and demonstrated the potential for a highly efficient hybrid recycling process.

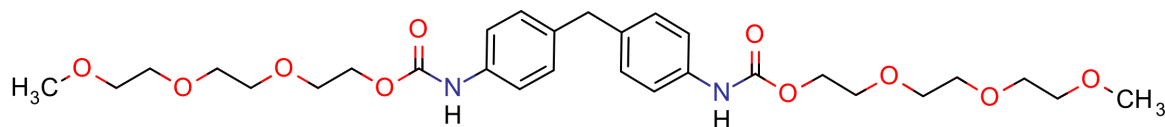
Nevertheless, it is desirable to further improve UMG-SP2's catalytic efficiency. Ideally, one should use the efficiency of the Carbios PET enzyme result as a reference¹⁵ and aim to engineer a urethanase that hydrolyzes 90% of thermoset PU materials within less than 24 h. To achieve this, the catalytic efficiency of UMG-SP2 must be improved. Here, we propose employing a rational design strategy, involving mutations based on a structure-to-activity relationship, to achieve this goal. To identify productive mutations rationally, the catalytic mechanism needs to be established, allowing the identification of "prejudicial residues" that

destabilize the rate-limiting transition state (TS) in relation to the reactant state. Such undesirable residues increase the reaction activation energy and consequently decrease the rate, making them the most promising targets for mutations aimed at enhancing UMG-SP2's catalytic efficiency.

UMG-SP2 belongs to the amidase signature superfamily, which has a highly conserved active site. Most members of this superfamily share the Ser_{nuc}-Ser_{cis}-Lys catalytic triad, including UMG-SP2 (Ser190_{nuc}-Ser166_{cis}-Lys91).¹⁷⁻¹⁹ In this type of catalytic triad, the mechanism typically starts with a proton transfer from Ser_{cis} to Lys, enabling the remaining Ser_{nuc} residue to perform a nucleophilic attack on the substrate's amide bond. For this to happen, the catalytic Lys must adopt a neutral state, as only in this state can it accept a proton donated by the Ser_{cis} residue. Later in the reaction, Lys returns the proton to Ser_{cis}, which in turn transfers its proton to the substrate's leaving group, culminating in the formation of the acyl-enzyme state and the release of an amine. To regenerate the enzyme, a water molecule enters the active site and conducts a nucleophilic attack on the acylated Ser_{nuc}. Consequently, the Ser_{nuc} residue becomes deacylated, releasing the product as a carboxylic acid, and the enzyme regenerates for a new catalytic cycle.²⁰

Recently, Li *et al.* (2024, "Structure-Guided Engineering of a Versatile Urethanase Improves Its Polyurethane Depolymerization Activity", submitted to *Advanced Science*) solved the X-ray structure of UMG-SP2. This provided significant structural insight into the UMG-SP2 catalysis, particularly regarding its regulation through the Loop 3 substrate-gating mechanism. However, the work of Li *et al.* primarily focused on enzyme activation. Enhancing substrate binding and the start of the catalysis should be complemented with more efficient catalysis. By combining easier activation with more efficient catalysis, the activity of UMG-SP2 towards PU substrates will significantly increase. Nevertheless, to improve the catalytic efficiency, the reaction mechanism should be studied. Even though the typical mechanism for Ser_{nuc}-Ser_{cis}-Lys has been studied before, the atomistic and energetic details vary throughout the family members. Additionally, to the best of our knowledge, the hydrolysis of the urethane bond catalyzed by this type of enzyme has not been elucidated. Thus, it is essential to study the catalytic mechanism of urethanases in detail, instead of relying on general studies for the amidase family. Moreover, the atomistic details of the rate-limiting TS are crucial for improving the catalytic efficiency of UMG-SP2. Therefore we set out to establish the mechanism of the urethane bond hydrolysis catalyzed by UMG-SP2 in order to propose

mutations to enhance its efficiency. For this purpose, we used the symmetric di-urethane ethylene 4,4'-Methylenedianiline (DUE-MDA) as a substrate (Scheme I).



Scheme I. The chemical structure of the PU substrate used in this work, di-urethane ethylene 4,4'-methylenedianiline (DUE-MDA).

This compound was chosen because it is a dicarbamate with two of the most often employed structural properties in industrial PU monomer formulations (MDA as the isocyanate and polyether as the polyol). We employed an adiabatic quantum mechanics/molecular mechanics methodology (QM/MM). Our calculations provided a detailed atomistic and energetic description of the mechanism and identified potential productive mutations to improve UMG-SP2's catalytic efficiency for urethane bond hydrolysis.

Methods

UMG-SP2 structure preparation:

We assembled the computational model used to explore the reaction mechanism of UMG-SP2 from the recently published X-ray structure of UMG-SP2 (PDB ID: 9FZW, 2.59 Å resolution; Li *et al.* 2024, “Structure-Guided Engineering of a Versatile Urethanase Improves Its Polyurethane Depolymerization Activity”, submitted to *Advanced Science*). Chain A and all crystallographic water molecules located within 10 Å of this chain (a total of 439 residues and 272 water molecules) were included in the model.

We estimated the protonation state of all residues, at pH 8.0, with the empirical pKa predictor PROPKA (version 3.5.0).²¹ PROPKA predicted that the side chains of the catalytic triad residues (Ser190_{nuc}-Ser166_{cis}-Lys91) should exist mostly in their neutral form (-NH₂ for Lys91, and -OH for the two serines). Visual inspection revealed that Lys91, buried in the active site cavity and therefore not solvated by water, was not close to any negatively charged residue (*i.e.*, Asp or Glu) that could stabilize a hypothetical positive state of this residue, thus explaining why PROPKA estimated a pKa value of 6.09. In its neutral form, the side chain of Lys91 was able to donate two hydrogen bonds to two nearby serine residues (Ser167 and Ser185, located at ≈ 3.0 -3.1 Å) and simultaneously accept a hydrogen bond from the catalytic Ser166_{cis} (2.35 Å). We further analysed visually the active site residues and other titratable residues in their surroundings to thoroughly verify the selected protonation states. Among the nine existing histidine residues, six were N_ε-protonated (His159, His196, His215, His271, His376, and His439), and three were N_δ-protonated (His108, His111, and His159).

Docking of the PU substrate and parameterization of the UMG-SP2:DUE-MDA complex:

Given that UMG-SP2 hydrolyzes low molecular weight dicarbamates of aromatic diamines (*e.g.*, toluene-2,4-diamine (TDA) and 4,4'-methyldianiline (MDA) derivatives),¹⁶ we decided to study the catalytic mechanism of this enzyme using the symmetric (DUE-MDA) compound. This ligand exhibits two urethane bonds on each side of the MDA core, each attaching a triethylene glycol monomethyl chain (Scheme I). We employed the GaussView 5.0 software²² to build the molecular structure of DUE-MDA, which was subsequently optimized with the Gaussian 09 software²³ at the HF/6-31G(d) level of theory. Then, the DUE-MDA ligand was docked to the active site of UMG-SP2 using the molecular docking software GOLD (Genetic Optimization Ligand Docking).²⁴ The binding region was defined as a 10 Å radius

sphere centered on the O_γ atom of the catalytic Ser190_{nuc}. We carried out the docking procedure using GOLD's automatic genetic algorithm settings with the search efficiency set to 100 %, and the results were scored using the CHEMPLP fitness function.²⁵ We thought it better to apply distance constraints to ensure an adequate positioning of the target urethane group regarding the active site residues. Specifically, the distances between the carbonyl oxygen of the urethane group and the NH_{backbone} groups of Ile187 and Gly188 were forced to lie within 1.5 and 3.0 Å (spring constant of 5.0). The docking procedure finished when the top three solutions laid within 1.5 Å RMSD (Root Mean Square Deviation) of each other. 10 different solutions were obtained, and we further performed a detailed analysis of the interatomic distances, hydrogen bonds, and close contacts between the docked ligand and the active site residues. In the end, we selected the solution that simultaneously exhibited the shortest O_γ(Ser190_{nuc})-C_{carbonyl}(DUE-MDA), O_{carbonyl}(DUE-MDA)-NH_{backbone}(Ile187), and O_{carbonyl}(DUE-MDA)-NH_{backbone}(Gly188) distances, to pursue the calculations.

Molecular Dynamics Simulations:

We neutralized the enzyme:ligand complex obtained from the docking procedure with Na⁺ counterions and placed it in the center of a rectangular box of TIP3P water molecules,²⁶ whose faces were at least 12 Å away from the enzyme's surface. This was accomplished by using the ANTECHAMBER module of AMBER 18.²⁷ In total, the system comprised 64,000 atoms. We obtained the molecular mechanics (MM) parameters for the DUE-MDA ligand from the *gaff2* force field,²⁸ and the MM parameters for the UMG-SP2 enzyme from the ff14SB force field.²⁹ On the other hand, the atomic charges of the ligand were derived from a restrained electrostatic potential fitting³⁰ performed at the HF/6-31G(d) level of theory with the Gaussian 09 software.

We employed the GROMACS software (version 2021.5)^{31, 32} to minimize the energy of the assembled system via a three-step protocol that used the steepest descent algorithm.³³ During the first minimization step, all water molecules were minimized. In the second step, the backbone atoms of UMG-SP2 were restrained while the remaining atoms of the system were minimized; in the final step, the whole system was minimized. The final minimized UMG-SP2 structure exhibited an RMSD of 0.38 Å (all enzyme non-hydrogen atoms were considered in the calculation) compared to the original crystallographic structure.

We then performed a classical molecular dynamics (MD) simulation to assess the overall stability of the UMG-SP2:DUE-MDA complex and to gather a structure that should correspond to a catalytically competent conformation. Throughout the entire MD protocol, all bonds involving hydrogen atoms were maintained fixed using the LINCS algorithm,³⁴ which

permitted the use of an integration time of 2 fs. The non-bonded interactions were explicitly calculated if under the cutoff of 10 Å, beyond which the Particle-Mesh Ewald scheme³⁵ was applied to treat non-bonded Coulomb interactions. The system was initially heated to 29 °C for 100 ps at constant volume conditions (*NVT* ensemble), which was accomplished by using the V-rescale thermostat³⁶ and by randomly generating initial velocities according to a Maxwell distribution. During this phase, all solute atoms were kept restrained. This heating phase was followed by a 2 ns-long *NPT* phase, in which the density of the solvent was relaxed at 1 bar and 29 °C, using the V-rescale thermostat and the Berendsen barostat.³⁷ Again, all solute atoms were kept fixed while the solvent was allowed to equilibrate.

Subsequently, we performed a 100 ns-long *NPT* phase to equilibrate the overall structure of the UMG-SP2 enzyme at 29 °C and 1 bar, while preserving the geometry of the active site residues (*i.e.*, Lys91, Ser166_{cis}, Ile187, Gly188, and Ser190_{nuc}) and the carbonyl group of the ligand's urethane bond with positional restraints. We followed this initial run with a second 100 ns-long *NPT* equilibration, which was conducted with fewer positional restraints (those affecting Ile187 and Gly188 were released). Finally, we carried out a 100 ns-long *NPT* production run without any restraints, controlling the temperature and pressure with the V-rescale thermostat and the Parrinello-Rahman barostat.³⁸ During this stage, we saved the configurations of the system every 200 ps, and followed five distances throughout the production phase. We used them as selection criteria to choose a catalytically competent UMG-SP2:DUE-MDA conformation: $H_{\gamma}(\text{Ser190}_{\text{nuc}})-O_{\gamma}(\text{Ser166}_{\text{cis}})$, $H_{\gamma}(\text{Ser166}_{\text{cis}})-N_{\zeta}(\text{Lys91})$, $O_{\gamma}(\text{Ser190}_{\text{nuc}})-C_{\text{carbonyl}}(\text{DUE-MDA})$, $O_{\text{carbonyl}}(\text{DUE-MDA})-\text{NH}_{\text{backbone}}(\text{Ile187})$, and $O_{\text{carbonyl}}(\text{DUE-MDA})-\text{NH}_{\text{backbone}}(\text{Gly188})$. The first three distances are related to the putative activation/deprotonation of the catalytic Ser190_{nuc} and the nucleophilic attack it should perform on the carbonyl carbon of the DUE-MDA's target urethane bond, respectively. The last two distances, calculated between two backbone amides and the ligand's carbonyl group, can be related to a successful accommodation of the target urethane bond in the cavity that hypothetically can act as an oxyanion hole throughout the enzymatic reaction. Configurations that exhibited interatomic distances inferior to 3.5 Å for $O_{\gamma}(\text{Ser190}_{\text{nuc}})-C_{\text{carbonyl}}(\text{DUE-MDA})$, and under 2.5 Å for the remaining four metrics were considered as being catalytically competent and potential candidates for the final UMG-SP2:DUE-MDA model. Approximately 32 % of all configurations fulfilled such criteria and we elected the top-ranked configuration (excluding the first 20 ns of the production phase, thus ensuring that a properly equilibrated structure was obtained) to pursue the QM/MM calculations.

QM/MM calculations:

We built the QM/MM model based on the structure gathered from the MD simulation, after removing the Na⁺ counterions and most of the solvent water molecules. The final QM/MM model encompassed the following selection: the entire UMG-SP2 enzyme, the complete DUE-MDA ligand, all water molecules within a 3 Å radius of the enzyme, and all water molecules within 6 Å of both the active site (Lys91, Ser166_{cis}, Ile187, Gly188, and Ser190_{nuc}) and the DUE-MDA ligand. We used this QM/MM model, with 9929 atoms, to study the catalytic mechanism of the acylation reaction (STAGE 1). The truncated system was split into two regions: quantum mechanics (QM) and molecular mechanics (MM). We treated the QM region with density-functional theory (DFT) and included the most relevant atoms for the reaction to be studied (Figure 1), *i.e.*: the complete Ser166_{cis}, Ser185, Gly188, Gly189, and Ser190_{nuc} residues; the complete side chain of Lys91; the complete Ser167, except its backbone carbonyl group; the backbone of Asp186 and Ile187; the backbone carbonyl groups of Gly165 and Gly184; the backbone amide groups of Ala141 and Ile191; the backbone of Leu140, except its amide group; a selection of 28 atoms of the DUE-MDA ligand, which includes the target urethane bond; and a single water molecule located nearby Ser185. In total, this region comprised 126 atoms, while the remaining 9803 atoms were included in the MM region and described at the *ff14SB* level of theory.

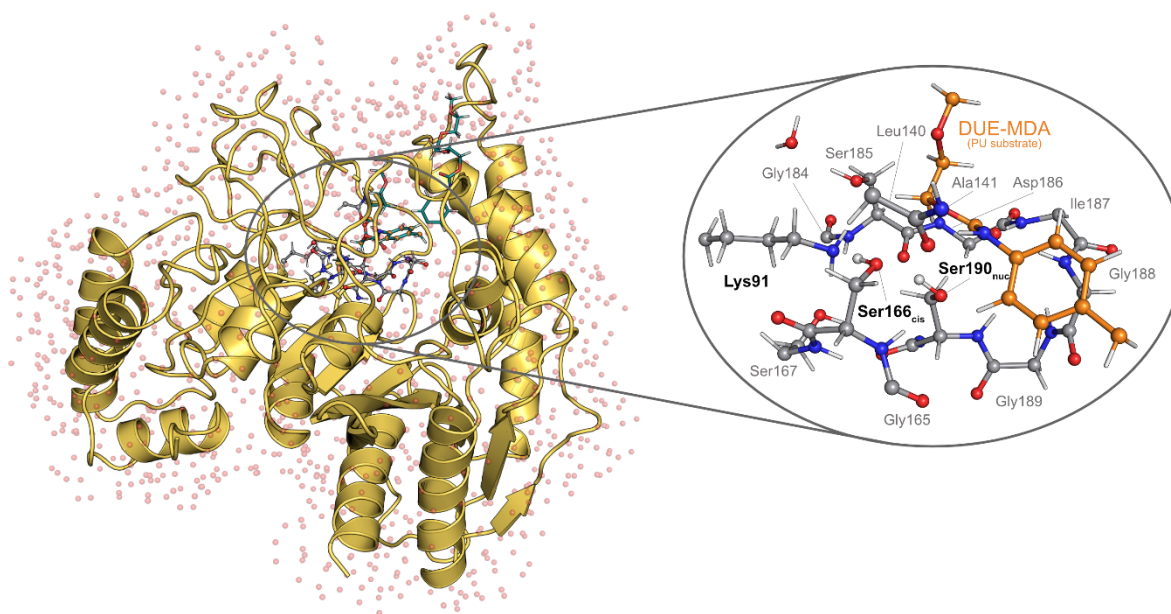


Figure 1. The QM/MM model used to study the catalytic mechanism of UMG-SP2. Left: cartoon representation of the UMG-SP2:DUE-MDA reactant structure (9929 atoms). The active site residues are represented as grey sticks, whereas the DUE-MDA substrate is shown as teal-colored sticks. Water molecules are

represented in red transparent spheres (hydrogen atoms are not shown for clarity purposes). Right: close-up of the QM region, composed of 126 atoms, shown in ball-and-stick representation. The PU substrate (DUE-MDA) is colored in orange. The Ser190_{nuc}-Ser166_{cis}-Lys91 catalytic triad is labeled in bold.

We continued our study using the ONIOM subtractive scheme³⁹ with electrostatic embedding in all QM/MM calculations, as implemented in the Gaussian 09 software. The valences of the bonds that crossed the boundary between the QM and MM layers were saturated with hydrogen atoms using the link-atom approach.^{40, 41} All of the solvent molecules located in the MM region were frozen using the molUP plugin for the VMD software.^{42, 43} The QM/MM model was initially optimized and later submitted to linear transit scans along putative reaction coordinates to investigate the steps underlying the catalytic mechanism. The linear transit scans' maxima were considered guesses for subsequent full transition state (TS) optimizations. Then, resorting to Intrinsic Reaction Coordinate (IRC) calculations, we obtained the minima associated with the optimized TSs, and their structure was subsequently optimized. We verified the nature of all stationary states as either TS (single imaginary frequency) or minima (absence of imaginary frequencies) with vibrational frequency calculations. All geometry optimizations, IRC, and vibrational frequency calculations were carried out using the B3LYP density functional^{44, 45} and the 6-31G(d) basis set. Single-point QM/MM energy calculations were conducted at the B3LYP/6-311+G(2d,2p)-D3(BJ):ff14SB level of theory in the fully optimized stationary states. Grimme's D3 dispersion with Becke-Johnson damping⁴⁶ was included in all calculations, as implemented in the Gaussian 09 software. The zero-point energy, as well as the thermal and entropic contributions to the Gibbs energy (calculated with the particle in a box/rigid rotor/harmonic oscillator formalism) were subsequently added to the final electronic energies of each stationary state to yield the corresponding Gibbs energy. Only vibrational temperatures larger than 120 K ($\approx 100 \text{ cm}^{-1}$) were considered for the calculation of entropic and enthalpic corrections, as validated elsewhere.⁴⁷

To determine whether the calculated Gibbs free energy profile is independent of the selected density functional, we conducted single-point calculations on the isolated QM layer of each stationary point using ORCA 4.2.1 software.⁴⁸ We employed B3LYP/6-311+G(2d,2p)-D3(BJ) and three additional theoretical methods: PWPB95, DSD-PBEB95, and SCS-MP2, all with the def2-TZVPP basis set. The energy difference between the three theoretical methods and B3LYP was then added as a correction to the QM/MM free energies previously calculated

with Gaussian 09, yielding the final Gibbs free energies, which are presented and discussed in Table S1 and Figure S1.

We studied the catalytic mechanism of the deacylation reaction (STAGE 2) using a similar procedure. We built the reactant state of the deacylation stage from the product of the acylation reaction after removing the leaving group, *i.e.*, the triethylene glycol monomethyl ether. The QM/MM system used to study the deacylation reaction comprised 9905 atoms, among which 117 formed the QM layer, and the remaining 9788 atoms were included in the MM region.

Finally, we obtained the reactant structure to start exploring the reactional state, from and after optimizing the assembled structure.

Per-residue contribution for the activation energy:

To improve the catalytic efficiency of UMG-SP2 towards PU substrates, we performed an energy reassessment study to evaluate the contribution of the surrounding MM residues to the reaction energetic barrier. We used the optimized structures of the associated stationary points for the rate-limiting step. We subjected the given stationary points to single-point energy calculations, each with a targeted MM residue deleted. This protocol was applied to a total of 149 residues, with all calculations being carried out at the B3LYP-D3BJ/6-311+G(2d,2p):ff14SB level of theory. The energy contribution of each residue to the barrier was given by the difference between the barrier obtained with the given residue deleted and the wild-type barrier. Therefore, a positive difference indicated that the residue increased the energetic barrier, whilst a negative difference indicated that the residue decreased the energetic barrier. This allows for mapping the energy contribution that each MM residue contributes to the barrier. Moreover, the residues which increase the energy barrier are the most promising mutational targets.

Results and Discussion

We retrieved the enzyme:ligand complex used in the mechanistic studies from the 100 ns-long MD simulation performed in this work. Throughout this simulation, the overall fold of UMG-SP2 remained stable, as shown by the RMSD analysis of the protein (Figure S2). by the RMSD for the enzyme's backbone of 1.29 ± 0.09 Å, considering the minimized structure as reference. Within this context, the docked DUE-MDA ligand also remained well-positioned for a catalytic reaction to occur: the carbonyl oxygen of the target urethane bond remained at, respectively, 2.33 ± 0.48 Å and 2.13 ± 0.37 Å of the proton of the backbone amides of Ile187 and Gly188, presumed to form the oxyanion hole; the carbonyl carbon of the same urethane bond remained, on average, at 3.22 ± 0.17 Å from the O_γ atom of Ser190_{nuc}, the nucleophilic species. A UMG-SP2:DUE-MDA conformation was selected from the MD simulation according to a set of distance-based criteria (methods section). The structural alignment of the chosen conformation and the original X-ray structure of UMG-SP2 (Li *et al.*, 2024, "Structure-Guided Engineering of a Versatile Urethanase Improves Its Polyurethane Depolymerization Activity", submitted to *Advanced Science*) (Figure S3) revealed that the two structures are very similar, both in their overall fold (backbone RMSD of 1.25 Å) and in the organization of the active site region (all-atom RMSD of 0.60 Å for the Lys91, Ser166_{cis}, Ser167, Ser185, Ile187, Gly188, and Ser190_{nuc} set of residues). Together, these findings highlight the quality and stability of the assembled UMG-SP2:DUE-MDA model.

STAGE 1: Enzyme Acylation and Cleavage of the Urethane Bond (Ester Part):

After an initial QM/MM geometry optimization, we obtained the final QM/MM model used to explore the chemical steps of the urethane bond cleavage of DUE-MDA by UMG-SP2, *i.e.* the reactant state - R. In the optimized model (Figure 2A), the carbonyl group of the target urethane bond simultaneously rested at 1.84 and 1.90 Å of the oxyanion hole amides and at 2.72 Å of the O_γ (Ser190_{nuc}) atom; the catalytic triad residues established a hydrogen bonding network between themselves, in which Lys91 acted as the hydrogen-bond acceptor of Ser166_{cis} (1.56 Å), and the latter as the acceptor of a hydrogen bond of Ser190_{nuc} (1.60 Å); two serine residues, Ser167 and Ser185, were hydrogen-bonded to the catalytic Lys91 (2.10 and 2.22 Å); Ser167 and Ser185 also acted as hydrogen-bond donors to the $O_{backbone}$ of Ser166_{cis} (1.89 and 2.23 Å) and a water molecule (1.88 Å), respectively (distances not shown in Figure 2A for clarity purposes); and the $O_{backbone}$ of Leu140 was at hydrogen-bonding distance to the NH group of the DUE-MDA's target urethane bond (distance not shown in Figure 2A for clarity

purposes). The latter was observed throughout the entire catalytic reaction (average distance of 1.98 Å).

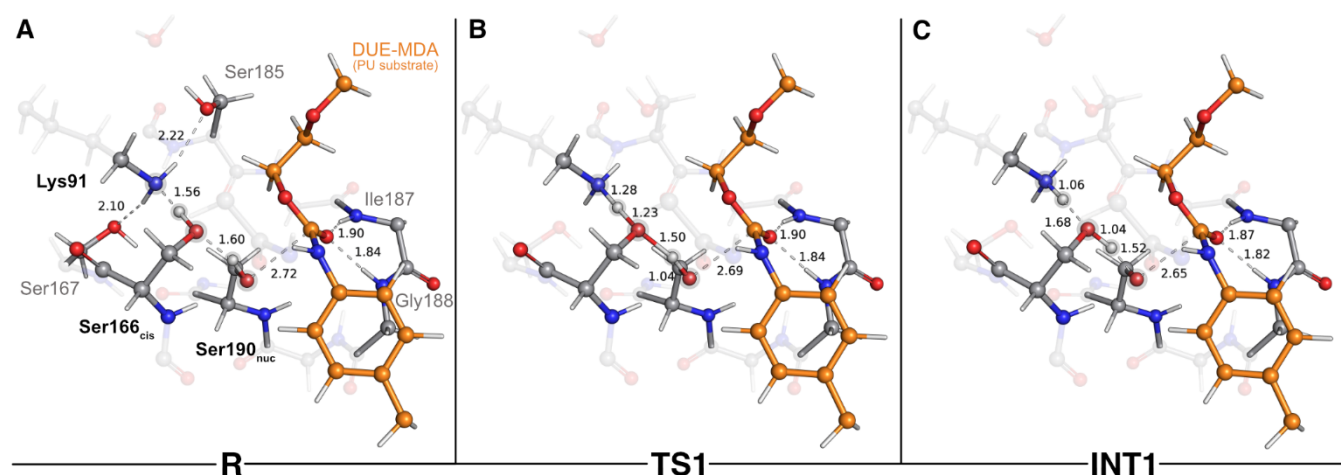


Figure 2. Optimized structures of the stationary states of the first catalytic step of UMG-SP2 (activation of Ser190_{nuc}). “R”, “TS1”, and “INT1” stand for reactant, first transition state, and first intermediate, respectively. The most important atoms for this catalytic step are highlighted by a grey shade. The PU substrate (DUE-MDA) is colored in orange. Some QM atoms are depicted as transparent sticks for clarity purposes. Relevant distances are given in Å.

As UMG-SP2 belongs to the amidase signature superfamily, we would expect that its catalytic reaction involved a nucleophilic attack mediated by the conserved Ser190_{nuc}-Ser166_{cis}-Lys91 triad. Our calculations revealed that before the attack on the target urethane bond of DUE-MDA takes place, the nucleophilic Ser190_{nuc} side chain hydroxyl must become activated, *i.e.* ionized. We observed that this occurs through a concerted and asynchronous reaction, in which Lys91 deprotonates Ser166_{cis}, thus activating it so that Ser166_{cis} in turn can abstract a proton from the nucleophilic Ser190_{nuc}. In the TS associated with this step (TS1, imaginary frequency of 909.1i cm⁻¹), the H_γ(Ser166_{cis}) was nearly equidistant to O_γ(Ser166_{cis}) and N_ζ(Lys91) (1.23 Å vs. 1.28 Å), whereas H_γ(Ser190_{nuc}) remained closer to its original position (1.04 Å to the Ser190_{nuc}'s O_γ) - Figure 2B. Throughout the concerted proton transfer, the O_γ(Ser190_{nuc}) builds up electron density and increases its negative character, as shown by the variation in its atomic charge when moving from the reactant (-0.22 a.u.) to the first intermediate state, INT1 (-0.33 a.u.). In the latter, the Bürgi-Dunitz angle, measured from Ser190_{nuc}'s side chain to the target urethane bond, adopted a value of 108°. Together, these findings reveal that the proton-transfer events rendered Ser190_{nuc} fully competent to conduct the attack on the substrate's carbonyl carbon. The calculations have shown that INT1 (Figure

2C) corresponds to a stationary state in the potential energy surface, but not to a minimum in the Gibbs free energy profile (activation Gibbs free energy of $0.3 \text{ kcal}\cdot\text{mol}^{-1}$ and reaction Gibbs free energy of $1.5 \text{ kcal}\cdot\text{mol}^{-1}$), meaning that it is not a stable intermediate of the reaction cycle. This suggests that the activation of Ser190_{nuc} should be concerted with the nucleophilic attack, although occurring in an early phase of the mechanistic step. Nevertheless, as the energy difference is very small, the enzyme should be able to easily switch between the two states.

Once activated, Ser190_{nuc} carried out the attack on the carbonyl carbon of the DUE-MDA's urethane bond (Figure 3). This reaction exhibited an activation Gibbs free energy (ΔG^\ddagger) of $17.4 \text{ kcal}\cdot\text{mol}^{-1}$, and it was endergonic in $16.0 \text{ kcal}\cdot\text{mol}^{-1}$. The TS of this catalytic step was characterized by an imaginary frequency of $151.1i \text{ cm}^{-1}$ (TS2 - Figure 3B) that was mostly associated with the stretching of the forming $\text{O}_\gamma(\text{Ser190}_{\text{nuc}})\text{-C}_{\text{carbonyl}}(\text{DUE-MDA})$ bond.

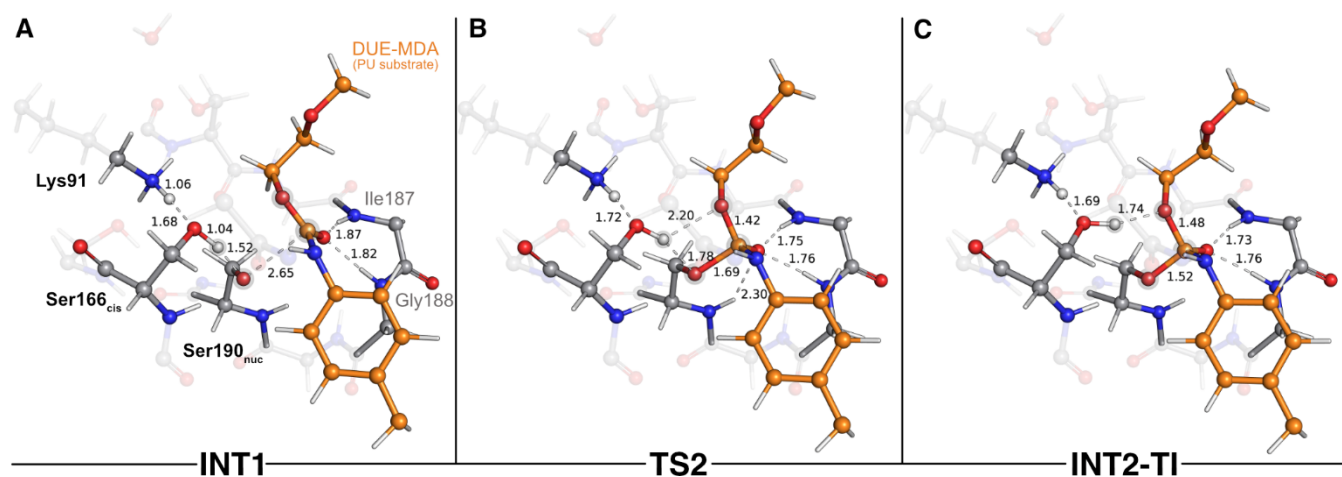


Figure 3. Optimized structures of the stationary states of the second catalytic step of UMG-SP2 (nucleophilic attack performed by Ser190_{nuc}). “INT1”, “TS2”, and “INT2-TI” stand for first intermediate, second transition state, and second intermediate-tetrahedral intermediate, respectively. The most important atoms for this catalytic step are highlighted by a grey shade. The PU substrate (DUE-MDA) is colored in orange. Some QM atoms are depicted as transparent sticks for clarity purposes. Relevant distances are given in Å.

As $\text{O}_\gamma(\text{Ser190}_{\text{nuc}})$ approached the substrate's carbonyl carbon (1.69 \AA in TS2), the negative character of the atoms that comprise the urethane bond increased, specifically that of $\text{O}_{\text{carbonyl}}$ atom (DUE-MDA), which changed from -0.28 a.u. (reactant) to -0.32 a.u. (TS2). The negative charge that built up on the carbonyl group was stabilized by the oxyanion hole backbone amide groups of Ile187 and Gly188 (*ca.* 1.76 \AA in TS2) and, to a lower extent, by the backbone amide group of the Ser190_{nuc} nucleophile (2.30 \AA in TS2). The calculations revealed that the product of this step corresponded to a tetrahedral intermediate (INT2-TI - Figure 3C), in which the

attacking Ser190_{nuc} was covalently bound to the DUE-MDA substrate (1.52 Å vs. 2.72 Å in the reactant state). In this stationary state, the substrate's carbonyl C-O bond exhibited a bond length (1.30 Å) that fell between those typical of single and double bonds, evidencing the increased negative character of this group. Consequently, it was in INT2-TI where the interactions with the oxyanion hole amide groups were stronger.

Throughout the nucleophilic attack, the ion-dipole interaction between Ser190_{nuc} and Ser166_{cis} became progressively weaker until it was lost in INT2-TI (Figure 3C). This occurred concomitantly to the establishment of a new hydrogen bond between Ser166_{cis} and the O_{ester} of the urethane bond under attack (1.74 Å in INT2-TI). As a result, Ser166_{cis} moved much closer to the urethane bond's O_{ester} than to its N_{amide} (1.74 Å vs. 3.10 Å), thus adopting a position that should favor the protonation of O_{ester}(DUE-MDA) rather than the N_{amide}(DUE-MDA) when the urethane bond breaking occurred. Such a role in facilitating the leaving group's protonation by the bridging Ser_{cis} of Ser_{nuc}-Ser_{cis}-Lys triads was also reported for other enzymes of the amidase signature superfamily, such as the fatty acid amide hydrolase.⁴⁹ The novelty here lies in the fact that Ser166_{cis} appears to play an important role in selecting which moiety should be first released as the leaving group. Specifically, our calculations showed that Ser166_{cis} cleaves the ester moiety rather than the amide side of the urethane bond, as we will discuss subsequently.

The next catalytic step involved the tetrahedral intermediate breakdown and the consequent cleavage of the urethane bond, concerted with a proton transfer from Ser166_{cis} to the O_{ester}(DUE-MDA), yielding an alcohol-leaving group (Figure 4). This step was characterized by a ΔG^\ddagger of 4.8 kcal·mol⁻¹ and was exergonic in -3.2 kcal·mol⁻¹.

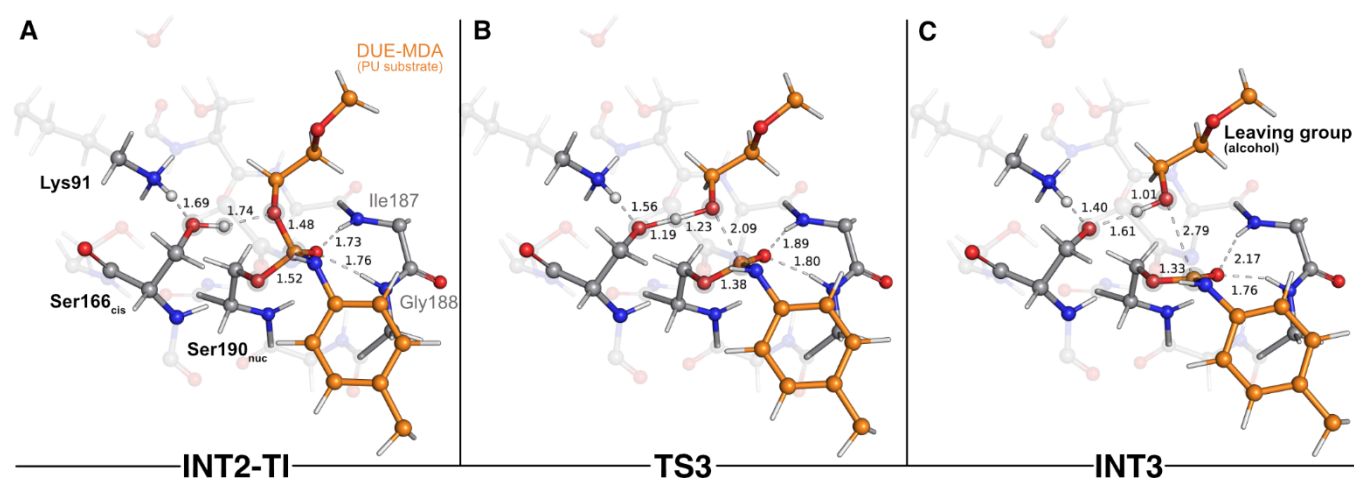


Figure 4. Optimized structures of the stationary states of the third catalytic step of UMG-SP2 (tetrahedral intermediate breakdown and urethane bond cleavage). “INT2-TI”, “TS3”, and “INT3” stand for second intermediate-tetrahedral intermediate, third transition state, and third intermediate, respectively. The most

important atoms for this catalytic step are highlighted by a grey shade. The PU substrate atoms are colored in orange. Some QM atoms are depicted as transparent sticks for clarity purposes. Relevant distances are given in Å.

As the reaction proceeded from INT2-TI to TS3 (Figure 4B), the $O_{\text{ester}}(\text{DUE-MDA})-C_{\text{carbonyl}}(\text{DUE-MDA})$ bond elongated from 1.48 Å to 2.09 Å and the substrate's carbonyl group became more positively charged. As a result, this group re-acquired the double bond character, its interactions with the oxyanion hole became weaker, and the $O_{\gamma}(\text{Ser190}_{\text{nuc}})-C_{\text{carbonyl}}(\text{DUE-MDA})$ bond shortened (1.52 Å in the INT2-TI vs. 1.38 Å in TS3). On the other hand, $O_{\text{ester}}(\text{DUE-MDA})$ built up electronic density (charge changed from -0.15 a.u. in INT2-TI to -0.25 a.u. in TS3) and became more prone to receive a proton from $O_{\gamma}(\text{Ser166}_{\text{cis}})$; in the TS3, the proton was virtually equidistant to both atoms (Figure 4B). The TS of this step was characterized by an imaginary frequency at $849.6i \text{ cm}^{-1}$ that was mostly dominated by the stretching of the atoms involved in the proton transfer. This indicates that, although concerted, the collapse of the tetrahedral intermediate (*i.e.*, urethane bond cleavage) preceded the proton transfer reaction, in an asynchronous event. When going from TS3 to the INT3 state (Figure 4C), the $O_{\text{ester}}(\text{DUE-MDA})-C_{\text{carbonyl}}(\text{DUE-MDA})$ bond became completely cleaved (2.79 Å), the proton was successfully transferred from Ser166_{cis} to the (now) alcohol-leaving group, and the $O_{\gamma}(\text{Ser190}_{\text{nuc}})$ became fully attached to the substrate's carbonyl carbon (1.33 Å). Moreover, the negative character of $O_{\gamma}(\text{Ser166}_{\text{cis}})$ increased substantially (-0.21 a.u. to -0.30 a.u.), which allowed it to become closer to the proton it previously transferred to Lys91 in the first catalytic step (1.40 Å in INT3).

The final step of the enzyme acylation stage consisted of a return of the proton from Lys91 to Ser166_{cis}, restoring their initial protonation state (Figure 5). Although we managed to characterize a transition state for this reaction (TS4, $841.7i \text{ cm}^{-1}$ - Figure 5B), our QM/MM calculations showed that the activation barrier required to go from INT3 to the final acyl-enzyme state (AE - Figure 5C) vanished upon the introduction of the thermal and entropic contributions to the Gibbs energy. This means that this catalytic step is barrierless and that once INT3 was formed, the proton transfer from Lys91 to Ser166_{cis} occurred spontaneously, yielding the AE with a reaction Gibbs free energy of $-1.9 \text{ kcal}\cdot\text{mol}^{-1}$. In the TS4 structure, the proton being shuttled to Ser166_{cis} was nearly halfway from the donor Lys91 residue (closer to Ser166_{cis} by 0.01 Å), and at the AE state the proton transfer was completed and both residues became neutral. The structural arrangement of these two states was virtually identical (all-atom RMSD

of the QM layer atoms of 0.07 Å), which explains their resemblance in energy terms (Gibbs free energy difference of just 0.1 kcal·mol⁻¹).

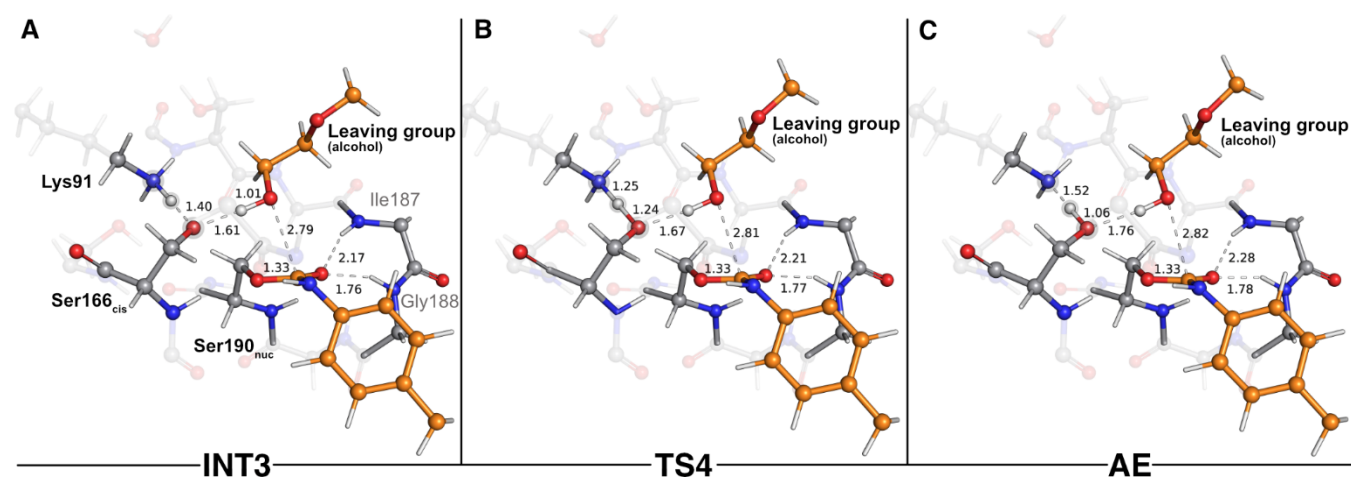


Figure 5. Optimized structures of the stationary states of the fourth catalytic step of UMG-SP2 (proton transfer from Lys91 to Ser166_{cis}). “INT3”, “TS4”, and “AE” stand for third intermediate, fourth transition state, and acyl-enzyme, respectively. The most important atoms for this catalytic step are highlighted by a grey shade. The PU substrate atoms are colored in orange. Some QM atoms are depicted as transparent sticks for clarity purposes. Relevant distances are given in Å.

After the acylation reaction, the resulting alcohol-leaving group, triethylene glycol monomethyl, was ready to abandon the active site, making it accessible to the solvent molecules required for the hydrolysis of the AE complex.

STAGE 2: Enzyme Deacylation and Complete Degradation of the Urethane Bond:

The second stage of the UMG-SP2 catalytic mechanism included the hydrolysis of the acyl-enzyme complex, product formation, and the regeneration of the Ser190_{nuc}-Ser166_{cis}-Lys91 triad. In the typical enzymatic hydrolyses of amide and ester bonds, the deacylation event is mediated by a water molecule that occupies the vacant space left by the leaving group, generated in the acylation stage.^{19, 20} Hence, after removing the alcohol-leaving group, we modeled a water molecule (Wat_{cat}) near the ester group of the acylated Ser190_{nuc} and subsequently performed a geometry optimization of the system. The gathered structure was used as the starting point to investigate the catalytic machinery behind the deacylation stage.

In the reactant state (AE* - Figure 6A), the catalytic water rested at 3.32 Å of the substrate’s carbonyl carbon, and its position was mainly dictated by the hydrogen bonds it established with Ser166_{cis} (1.85 Å) and with Ser185 (2.15 Å). Similarly to the reactant state of the acylation stage (R - Figure 2A), Lys91 acted as a hydrogen bond donor to Ser167 (2.01 Å) and Ser185

(2.15 Å), while simultaneously being an acceptor of a strong hydrogen bond from Ser166_{cis} (1.54 Å). The substrate's carbonyl group remained lodged in the oxyanion hole cavity (at 1.79 and 2.20 Å of the amide groups) and interacted with the backbone amide of Ser190_{nuc} (2.04 Å).

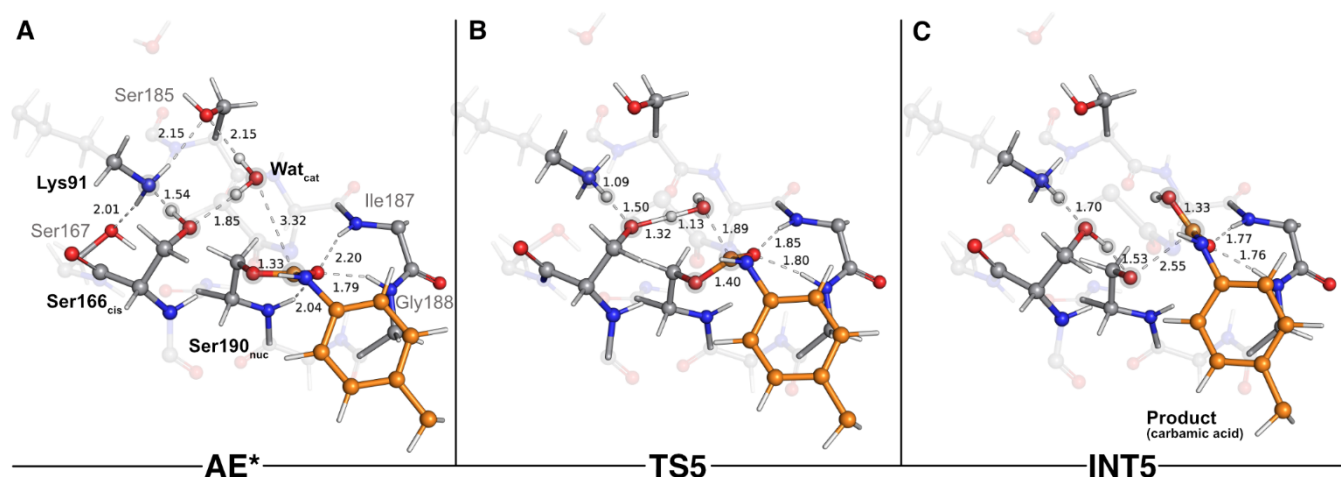


Figure 6. Optimized structures of the stationary states of the fifth catalytic step of UMG-SP2 (concerted activation of Wat_{cat} and nucleophilic attack). “AE*”, “TS5”, and “INT5” stand for acyl enzyme/reactant (stage 2), fifth transition state, and fifth intermediate, respectively. The most important atoms for this catalytic step are highlighted by a grey shade. The PU substrate atoms are colored in orange. Some QM atoms are depicted as transparent sticks for clarity purposes. Relevant distances are given in Å.

The first step of the deacylation stage consisted of a concerted reaction that combined three elementary steps: a proton transfer from Ser166_{cis} to Lys91, a second proton transfer from Wat_{cat} to Ser166_{cis}, and a nucleophilic attack conducted by the Wat_{cat} on the carbonyl carbon of the acylated Ser190_{nuc}. This step was characterized by a ΔG^\ddagger of 17.8 kcal·mol⁻¹ and was exergonic in -6.0 kcal·mol⁻¹. Despite the concerted nature of these catalytic events, our calculations showed that they occurred asynchronously, as discussed below. The transition state of this step (TS5 - Figure 6B) was characterized by an imaginary frequency at 403.3i cm⁻¹, which was largely dominated by the stretching of the O(Wat_{cat})-C_{carbonyl}(DUE-MDA) and H(Wat_{cat})-O_γ(Ser166_{cis}) bonds. In this state, the proton transfer from Ser166_{cis} to Lys91 was completed (1.09 Å vs. 1.54 Å in the AE* state), the Wat_{cat} shared one of its hydrogen atoms with Ser166_{cis} (1.32 Å vs. 1.85 Å in the AE* state), and the nucleophilic O(Wat_{cat}) rested at 1.89 Å from the target carbonyl carbon atom. This indicated that, within the same catalytic step, the activation of Ser166_{cis} by Lys91 preceded the remaining two events. We believe that this should be required for Ser166_{cis} to build up more electronic density on its side chain oxygen (charge changed from -0.24 a.u. to -0.28 a.u. from AE* to TS5) and to become more prone to activate the nucleophilic Wat_{cat}.

As the reaction proceeded from TS5 to INT5 (Figure 6C), the hydroxyl group originating from Wat_{cat} became bound to the substrate's carbonyl carbon (1.33 Å in the INT5 structure), and the bond between O_γ(Ser190_{nuc}) and the substrate was cleaved (2.55 Å in INT5 vs. 1.40 Å in TS5). In the acylation stage, we characterized a tetrahedral intermediate that originated from Ser190_{nuc}'s nucleophilic attack on the carbonyl group of the substrate's urethane bond (INT2-TI - Figure 3C). However, in the current stage, we did not observe the formation of a stable tetrahedral intermediate resulting from the nucleophilic attack conducted by Wat_{cat}. Indeed, the IRC calculation performed to obtain INT5 from TS5 showed that the system passed through a tetrahedral geometry that immediately decayed to the INT5 state, and that, during this process, Ser190_{nuc} became deacylated and the product was released in the form of a carbamic acid (Figure 6C). Furthermore, it also revealed that the negative character of the O_γ(Ser190_{nuc}) atom increased as Ser190_{nuc} became deacylated (charge varied from -0.13 a.u. in the TS5 to -0.32 a.u. in the INT5), which induced the establishment of a new ion-dipole interaction with Ser166_{cis} (1.53 Å), specifically with the hydrogen atom that Ser166_{cis} previously received from Wat_{cat}.

The second step of the deacylation stage concluded the overall catalytic mechanism of UMG-SP2. It corresponded to the regeneration of the enzyme's initial state and proceeded via two concerted and asynchronous proton transfers between the residues of the Ser190_{nuc}-Ser166_{cis}-Lys91 triad (Figure 7): Ser166_{cis} shuttled a proton to Ser190_{nuc} and accepted a proton from Lys91 (the one transferred in the opposite direction during the previous catalytic step). A closer look at the TS of this reaction (TS6 - Figure 7B) revealed that when the proton was nearly halfway from Lys91 and Ser166_{cis} (1.30 Å to Lys91 and 1.21 Å to Ser166_{cis}), the bond between O_γ(Ser190_{nuc}) and the proton transferred from Ser166_{cis} was already established (1.05 Å), corroborating the asynchronous nature of these events. TS6 exhibited a single imaginary frequency at 822.0i cm⁻¹, largely dominated by the stretching of the atoms involved in the proton transfer between Lys91 and Ser166_{cis}.

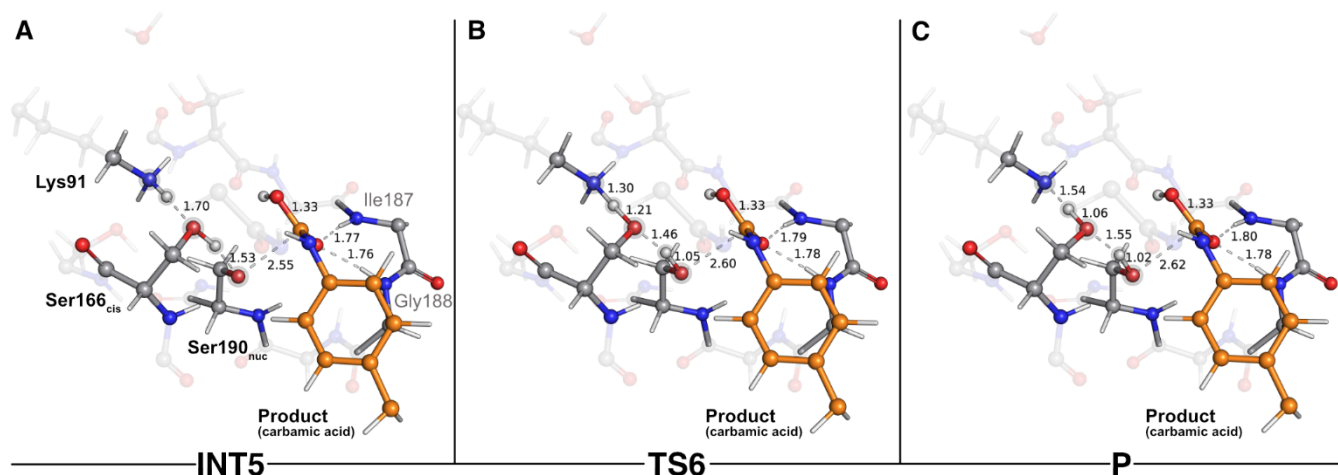


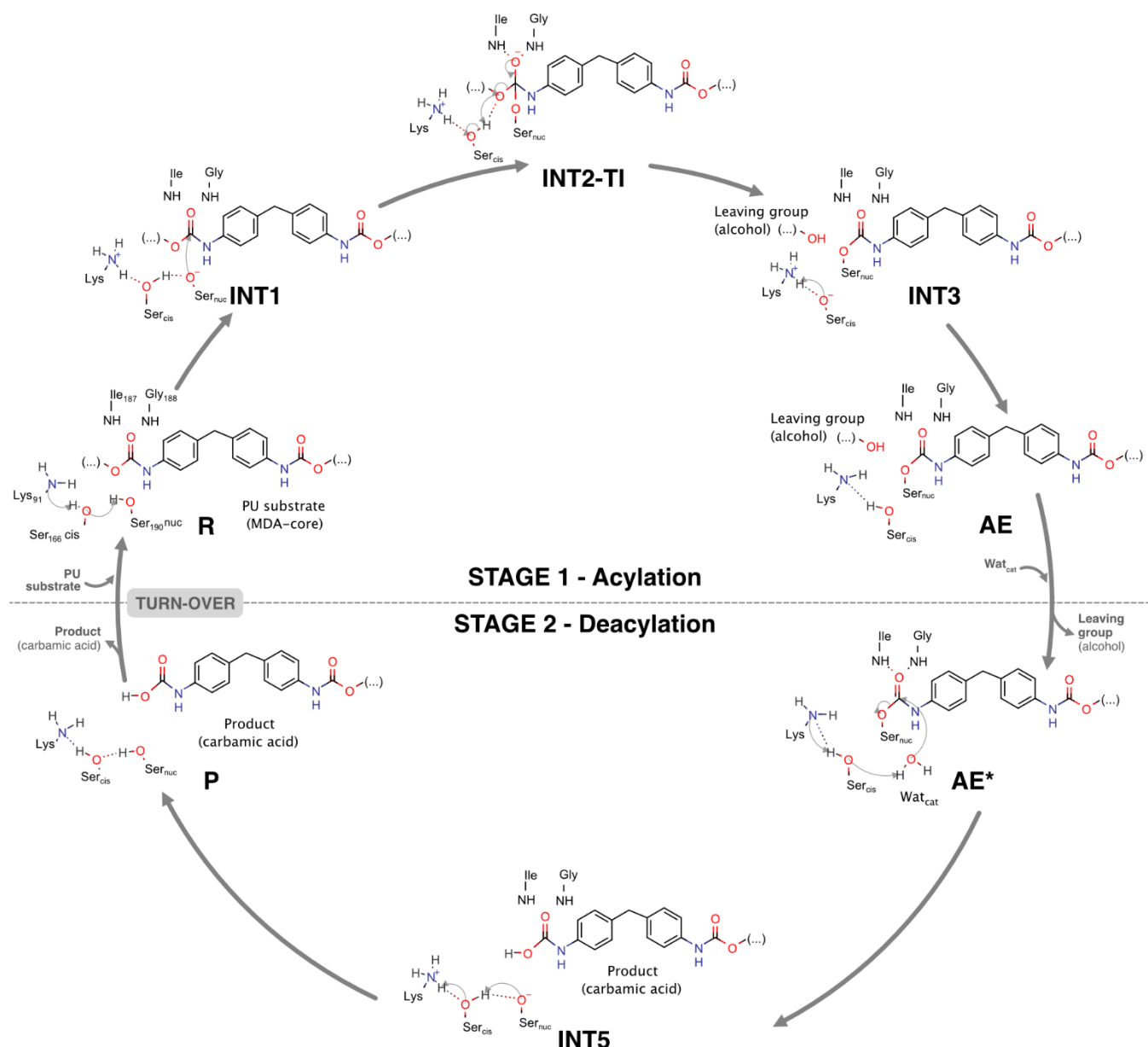
Figure 7. Optimized structures of the stationary states of the sixth catalytic step of UMG-SP2 (regeneration of the catalytic triad). “INT5”, “TS6”, and “P” stand for fifth intermediate, sixth transition state, and product, respectively. The most important atoms for this catalytic step are highlighted by a grey shade. The PU substrate atoms are colored in orange. Some QM atoms are depicted as transparent sticks for clarity purposes. Relevant distances are given in Å.

The calculations revealed that this reaction led to a state (P - Figure 7C) that corresponded to a minimum in the potential energy surface, but not to a stable intermediate in the thermal Gibbs free energy profile ($\Delta G^\ddagger = 0.5 \text{ kcal}\cdot\text{mol}^{-1}$ and $\Delta G_{\text{reaction}} = 1.6 \text{ kcal}\cdot\text{mol}^{-1}$). This phenomenon was also observed in the first catalytic step of the entire mechanism, where we hypothesized that the enzyme should be able to easily switch between the charged ($\text{Ser190}_{\text{nuc}}^-$ - $\text{Ser166}_{\text{cis}}$ - Lys91^+ , observed in INT1) and neutral ($\text{Ser190}_{\text{nuc}}$ - $\text{Ser166}_{\text{cis}}$ - Lys91 , observed in R) states. We believe that the same applies in this step and that both states are interchangeable.

Overall Reaction Cycle of UMG-SP2:

Scheme II and Figure 8 depict the complete catalytic mechanism and the global Gibbs free energy profile for the cleavage of one urethane bond of the PU substrate DUE-MDA by UMG-SP2.

Scheme II – The complete catalytic mechanism for the cleavage of one urethane bond by UMG-SP2.



The catalytic reaction occurred in two well-defined stages: in STAGE 1, the enzyme became covalently bound to the PU substrate, and an alcohol-leaving group was released; in STAGE 2, the enzyme:ligand covalent adduct was hydrolyzed by a catalytic water molecule and the product was released in the form of a carbamic acid (Scheme I).

According to Figure 8, the complete catalytic reaction required a Gibbs activation free energy of $20.8 \text{ kcal}\cdot\text{mol}^{-1}$. Even though the turnover rate for this enzyme has not been reported, we find reassurance in the fact that the theoretically calculated energy barrier laid within the range of values ($\sim 13\text{-}23 \text{ kcal}\cdot\text{mol}^{-1}$) corresponding to the experimental catalytic rates of most known hydrolases.⁵⁰ The rate-limiting transition state of the overall reaction (TS3)

corresponded to the concerted reaction that combined the tetrahedral intermediate breakdown and the cleavage of the substrate's urethane bond by its ester moiety with the subsequent formation of the alcohol-leaving group.

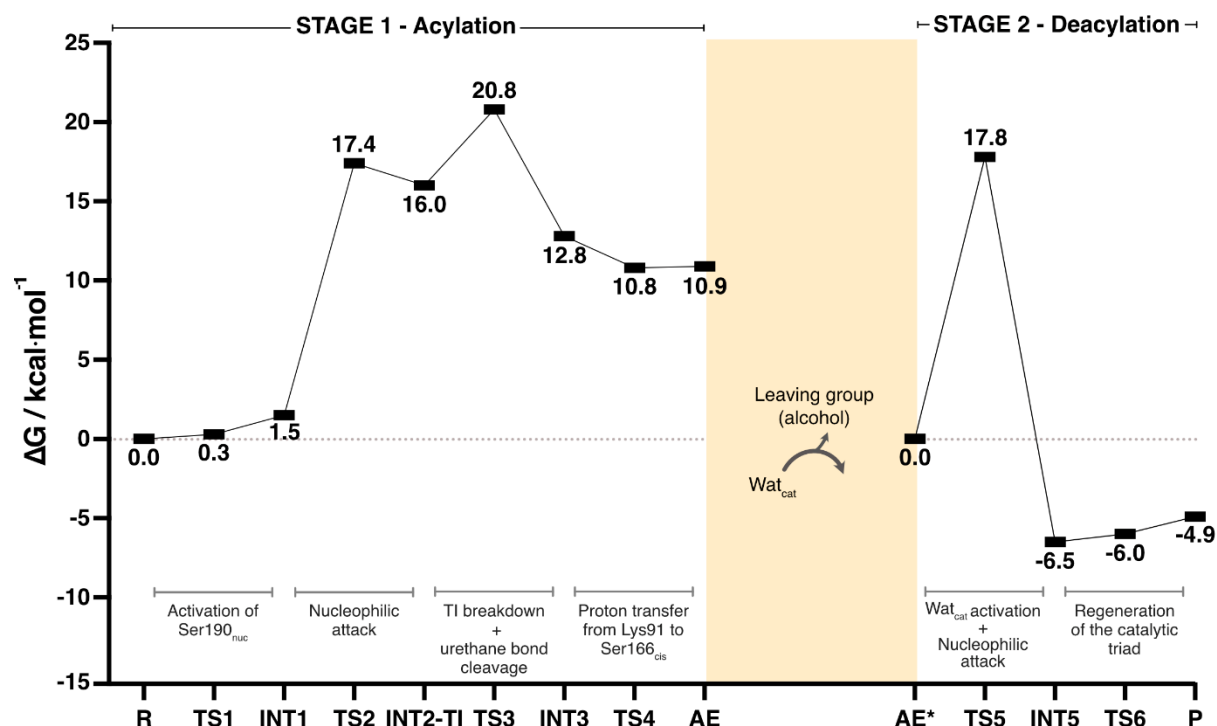


Figure 8 – The global Gibbs free energy profile for the cleavage of one urethane bond by UMG-SP2. The presented ΔG values were determined at the B3LYP/6-311+G(2d,2p)-D3(BJ):*ff*14SB//B3LYP/6-31G(d)-D3(BJ):*ff*14SB level of theory and are presented in kcal·mol⁻¹. The energy profiles of each stage are shown separately. Connecting the Gibbs energy profiles of the two stages requires complex and often inaccurate calculations of the Gibbs energy for the alcohol-leaving group dissociation and active site solvation, that being why we adopted the current representation. Each mechanistic step is indicated in the bottom part of the plot, in dark grey.

Our calculations revealed that a carbamic acid product resulted from the urethane bond cleavage of DUE-MDA by UMG-SP2. Carbamic acids are known to be unstable at room temperature and to quickly decompose to form an amine and carbon dioxide (CO₂).^{51, 52} Therefore, we believe the product we characterized should quickly eliminate CO₂ and give rise to a monosubstituted MDA-urethane compound, specifically mono-urethane ethylene 4,4'-methylenedianiline (MUE-MDA). A second catalytic cycle of UMG-SP2 would complete the cleavage of the remaining urethane bond of MUE-MDA, releasing the alcohol-leaving group, triethylene glycol monomethyl, and the carbamic acid form of 4,4'-methylenedianiline (MDA). Again, the latter should quickly decompose into CO₂ and MDA (the amine), which,

interestingly, was detected as the end product of UMG-SP1's activity on a synthetic MDA diisocyanate-based thermoplastic polyester-PU.⁵³

Contribution of individual residues to the activation energy

Even though the UMG-SP2 has shown considerable activity towards dicarbamates (PU monomers), there is still room to enhance its efficiency with this substrate. The catalytic efficiency is influenced by k_{cat} and K_{M} , and we focus here on k_{cat} , which is typically calculated with greater accuracy and is a primary target in directed evolution. As it is known that k_{cat} is related to the energy barrier, we calculated the energy contribution of each surrounding MM residue to the energy barrier to identify mutations that could enhance the catalytic efficiency by improving the k_{cat} . Rate-limiting steps involving significant electron density rearrangements are stabilized or destabilized by surrounding charged residues. This effect is dependent on the nature of the active site macrodipole and the positioning of these residues within the active site.⁵⁴⁻⁵⁶

By definition, residues that destabilize the rate-limiting TS (TS3) in relation to the reactant state increase the energy barrier, while those that stabilize it will decrease the barrier. Based on the nature of TS3 and the reactant state, we predict that positive residues closer to the $\text{O}_{\text{ester}}(\text{DUE-MDA})$ than to the $\text{O}_{\gamma}(\text{Ser190}_{\text{nuc}})$ will stabilize the TS3 in relation to the reactant state. Conversely, positive residues nearer the $\text{O}_{\gamma}(\text{Ser190}_{\text{nuc}})$ will do the opposite. For negative residues, those closer to the $\text{O}_{\gamma}(\text{Ser190}_{\text{nuc}})$ are expected to stabilize TS3 in relation to the reactant state, while those nearer to the $\text{O}_{\text{ester}}(\text{DUE-MDA})$ will do the opposite. The residues that destabilize TS3 are the most promising targets for mutation.

Figure 9 shows the impact of each deleted MM residue on the energy barrier. Additionally, the energy contribution of each residue is plotted as a function of the difference between the distance to the positive side of the TS3 macrodipole ($\text{O}_{\gamma}(\text{Ser190}_{\text{nuc}})$) and the distance to the negative side ($\text{O}_{\text{ester}}(\text{DUE-MDA})$). For this measurement, we assigned a reference carbon atom for each type of residue (Table S2).

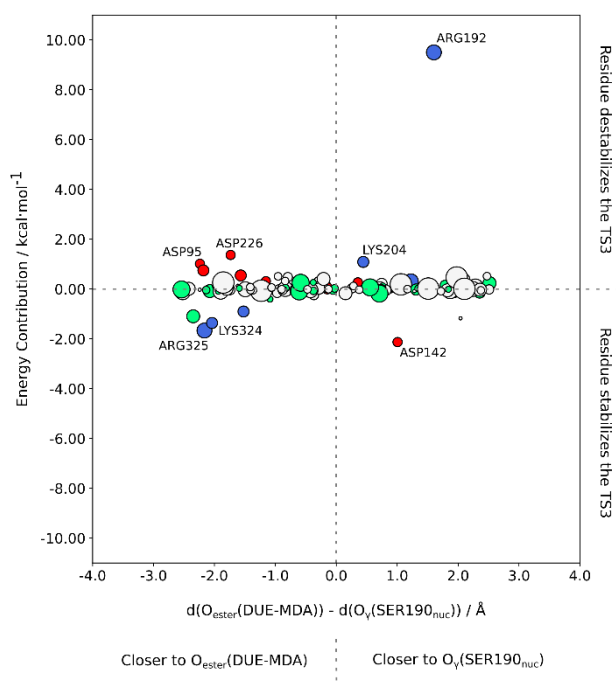


Figure 9. The impact of each surrounding MM residue on the reaction energy barrier as a function of the difference between the distance of the given MM residue to the positive ($O_{\gamma}(\text{Ser190}_{\text{nuc}})$) and the negative sides ($O_{\text{ester}}(\text{DUE-MDA})$) of the TS3 macrodipole. Positive residues are colored blue, while negative residues are colored red. Polar residues are colored green, and hydrophobic residues are colored white. Only the residues that have a relevant energy contribution (*e.g.*, $|1.0| \text{ kcal mol}^{-1}$) are identified. The top half of the graph shows the residues that destabilize TS3, *i.e.* the most promising targets for mutation.

We observed that most residues with a significant energy contribution to the barrier were charged. Additionally, the majority of those charged residues were closer to the $O_{\text{ester}}(\text{DUE-MDA})$ than to $O_{\gamma}(\text{Ser190}_{\text{nuc}})$. Furthermore, most negative residues were located closer to the negative side of the TS3 macrodipole. Consistent with our prediction, residues Asp95 and Asp226 destabilized TS3, leading to an increase of the energy barrier. Since these residues were closer to the negative side of the TS3 macrodipole, we suggest mutating them to polar residues (*e.g.*, Asn) for a more conservative strategy, or to positive residues (Lys or Arg) for a structurally riskier approach. Conversely, Asp142 was closer to $O_{\gamma}(\text{Ser190}_{\text{nuc}})$ than to $O_{\text{ester}}(\text{DUE-MDA})$, placing it closer to the positive side of the TS3 macrodipole, thereby lowering the energy barrier.

We also predicted that positive residues closer to the $O_{\text{ester}}(\text{DUE-MDA})$ than to $O_{\gamma}(\text{Ser190}_{\text{nuc}})$ stabilize the TS3, contributing to a lower energy barrier. In line with our rationale, Lys324 and Arg325, located near the negative side of the macrodipole, stabilized

TS3. On the other hand, we predicted that positive residues closer to the O_{γ} (Ser190_{nuc}) than to O_{ester} (DUE-MDA) destabilize TS3. Accordingly, Arg192 and Lys204, being near the positive side of the TS3 macrodipole, destabilized TS3. Notably, Arg192 significantly increased the energy barrier, making it the most promising mutational target. Arg192 was surrounded by neutral residues, with a lack of strong electrostatic interactions in its vicinity. The absence of stabilizing interactions for the positive charge resulted in the destabilization of its surroundings. This charged residue was close to the backbone of Ser190_{nuc}, Ile187, and Gly188, which are key residues for the reaction, meaning their stability is essential. The presence of a nearby unstable positive charge in the vicinity of these residues led to their destabilization, consequently destabilizing TS3. Hence, Arg192 should be mutated to a polar or hydrophobic residue (*e.g.*, Gln, His, or Met) to stabilize the neutral residue network. Concerning Lys204, as it is closer to the positive side of the TS3 macrodipole, we propose mutating it to a neutral residue (*e.g.*, Gln or Met) for a more conservative strategy or to a negative residue (*e.g.*, Asp or Glu) for a more aggressive strategy.

Based on our method, we believe that mutating the four aforementioned targets should stabilize the TS3 macrodipole. This stabilizing effect will lower the energy barrier, leading to an increase in the k_{cat} term, achieving our goal of improving the UMG-SP2 hydrolysis of PU substrates.

Conclusion

In this work, we investigated the hydrolysis of a model substrate of PU (DUE-MDA), catalyzed by the metagenome-derived UMG-SP2 enzyme. We employed computational methods to unveil, with atomic detail, the catalytic machinery behind this enzymatic reaction and determined its overall Gibbs free energy profile (Figure 8).

Our calculations demonstrated that UMG-SP2 cleaves urethane bonds in two mechanistic stages, acylation and deacylation, and that the first comprises the rate-limiting step with an overall ΔG^\ddagger of 20.8 kcal·mol⁻¹. The catalytic cycle culminates with the release of the final product in the form of a carbamic acid (Figure 8A). Strictly speaking, the enzyme does not fully degrade the target urethane bond, but rather cleaves its ester moiety (esterase-like activity), leading to a highly unstable product. The latter should, in an enzyme-independent manner, rapidly decompose to form CO₂ and an amine, causing the complete degradation of the urethane bond.

The QM/MM calculations shed light on the specific role of the active site residues during the urethane bond hydrolysis. They corroborated that Ser190_{nuc} is the nucleophile, whose reactivity is controlled by the remaining two residues of the catalytic triad (Lys91 and Ser166_{cis}). Lys91 establishes persistent hydrogen bond interactions with two nearby residues (Ser167 and Ser185) and, by deprotonation/protonation events, respectively activates/deactivates the bridging Ser166_{cis}. The latter acts as a catalytic base, activating the nucleophilic Ser190_{nuc}, and is also responsible for the protonation of the substrate's leaving group. In addition, Ser166_{cis} plays a major role in selecting which moiety (ester vs. amine) should be released as the leaving group. The structural rearrangement of Ser166_{cis}'s side chain during the nucleophilic attack by Ser190_{nuc} facilitates the proton transfer to O_{ester}(DUE-MDA) and the subsequent urethane bond cleavage by its ester side. Throughout these events, the enzyme's oxyanion hole accommodates the urethane bond's carbonyl and stabilizes the tetrahedral reaction intermediates.

Finally, we have identified four mutational targets predicted to stabilize the TS3 macrodipole, which are expected to decrease the energy barrier and enhance the catalytic efficiency of UMG-SP2 for urethane bond cleavage.

Overall, the findings reported herein offer valuable insight into the catalytic mechanism underlying the hydrolysis of PU substrates by UMG-SP2. We hypothesize that, to some extent, many of the reported phenomena may be common to the other two metagenomic urethanases (UMG-SP1 and UMG-SP3) and to other enzymes of the amidase signature superfamily,

although further studies are needed to corroborate this assumption. We hope this work encourages future research on the enzymatic depolymerization of PU that aims to address the environmental issues arising from the widespread use of plastics.

Supporting Information

This information is available free of charge on the ACS Publications website:

Free energy profiles for the UMG-SP2-catalyzed reaction, determined at different theoretical levels; Gibbs activation energy values, determined at different theoretical levels; RMSD fluctuation of the protein during the 100 ns-long production phase; Structural alignment of the X-ray and the MD-gathered UMG-SP2 structures; List of the reference atoms used to assess the contribution of individual residues to the activation energy (PDF)

Acknowledgements

The authors would like to thank the EnZync consortium, and the financial support received by the Novo Nordisk Fonden, under project NNF22OC0072891 (Challenge Programme 2022 - Recycling or a Sustainable Society). P.P., P.A.F. and M.J.R. acknowledge the financial support of FCT/MCTES (LA/P/0008/2020 DOI 10.54499/LA/P/0008/2020, UIDP/50006/2020 DOI 10.54499/UIDP/50006/2020 and UIDB/50006/2020 DOI 10.54499/UIDB/50006/2020), through national funds. The European High-Performance Computing Joint Undertaking (EuroHPC JU) that granted us access to MeluXina, the petascale EuroHPC supercomputer located in Bissen, Luxembourg, under proposal EHPC-REG-2023R03-163, is gratefully acknowledged.

Author contributions

PP and LT performed the calculations. PAF and MJR supervised them. All authors contributed to the writing of the manuscript. The paper has been approved in its final form by all authors.

Competing interests

The authors declare that they have no competing interests.

References

- (1) Walker, T. R.; Fequet, L. Current trends of unsustainable plastic production and micro(nano)plastic pollution. *TrAC, Trends Anal. Chem.* **2023**, *160*, 116984. DOI: <https://doi.org/10.1016/j.trac.2023.116984>.
- (2) Prata, J. C.; Silva, A. L. P.; da Costa, J. P.; Mouneyrac, C.; Walker, T. R.; Duarte, A. C.; Rocha-Santos, T. Solutions and Integrated Strategies for the Control and Mitigation of Plastic and Microplastic Pollution. *Int. J. Environ. Res. Public Health* **2019**, *16* (13). DOI: 10.3390/ijerph16132411 From NLM Medline.
- (3) PlasticsEurope. *Plastics – the fast Facts 2023*; 2023.
- (4) Karbalaei, S.; Hanachi, P.; Walker, T. R.; Cole, M. Occurrence, sources, human health impacts and mitigation of microplastic pollution. *Environ. Sci. Pollut. Res. Int.* **2018**, *25* (36), 36046-36063. DOI: 10.1007/s11356-018-3508-7 From NLM Medline.
- (5) Magnin, A.; Pollet, E.; Phalip, V.; Averous, L. Evaluation of biological degradation of polyurethanes. *Biotechnol. Adv.* **2020**, *39*, 107457. DOI: 10.1016/j.biotechadv.2019.107457 From NLM Medline.
- (6) de Souza, F. M.; Kahol, P. K.; Gupta, R. K. Introduction to Polyurethane Chemistry. In *Polyurethane Chemistry: Renewable Polyols and Isocyanates*, ACS Symposium Series, Vol. 1380; American Chemical Society, 2021; pp 1-24.
- (7) Rossignolo, G.; Malucelli, G.; Lorenzetti, A. Recycling of polyurethanes: where we are and where we are going. *Green Chem.* **2024**, *26* (3), 1132-1152, 10.1039/D3GC02091F. DOI: 10.1039/D3GC02091F.
- (8) European, C.; Joint Research, C.; Nessi, S.; Garcia-Gutierrez, P.; Tonini, D. *Environmental effects of plastic waste recycling*; Publications Office of the European Union, 2021. DOI: doi/10.2760/6309.
- (9) Kemon, A.; Piotrowska, M. Polyurethane Recycling and Disposal: Methods and Prospects. *Polymers (Basel)* **2020**, *12* (8). DOI: 10.3390/polym12081752 From NLM PubMed-not-MEDLINE.
- (10) Mohanan, N.; Montazer, Z.; Sharma, P. K.; Levin, D. B. Microbial and Enzymatic Degradation of Synthetic Plastics. *Front. Microbiol.* **2020**, *11*, 580709. DOI: 10.3389/fmicb.2020.580709 From NLM PubMed-not-MEDLINE.
- (11) Yoshida, S.; Hiraga, K.; Takehana, T.; Taniguchi, I.; Yamaji, H.; Maeda, Y.; Toyohara, K.; Miyamoto, K.; Kimura, Y.; Oda, K. A bacterium that degrades and assimilates

poly(ethylene terephthalate). *Science* **2016**, *351* (6278), 1196-1199. DOI: 10.1126/science.aad6359 From NLM Medline.

(12) Burgin, T.; Pollard, B. C.; Knott, B. C.; Mayes, H. B.; Crowley, M. F.; McGeehan, J. E.; Beckham, G. T.; Woodcock, H. L. The reaction mechanism of the *Ideonella sakaiensis* PETase enzyme. *Commun Chem* **2024**, *7* (1), 65. DOI: 10.1038/s42004-024-01154-x From NLM PubMed-not-MEDLINE.

(13) Liu, F.; Wang, T.; Yang, W.; Zhang, Y.; Gong, Y.; Fan, X.; Wang, G.; Lu, Z.; Wang, J. Current advances in the structural biology and molecular engineering of PETase. *Front Bioeng Biotechnol* **2023**, *11*, 1263996. DOI: 10.3389/fbioe.2023.1263996 From NLM PubMed-not-MEDLINE.

(14) Schwaminger, S. P.; Fehn, S.; Steegmüller, T.; Rauwolf, S.; Löwe, H.; Pflüger-Grau, K.; Berensmeier, S. Immobilization of PETase enzymes on magnetic iron oxide nanoparticles for the decomposition of microplastic PET. *Nanoscale Advances* **2021**, *3* (15), 4395-4399, 10.1039/D1NA00243K. DOI: 10.1039/D1NA00243K.

(15) Tournier, V.; Topham, C. M.; Gilles, A.; David, B.; Folgoas, C.; Moya-Leclair, E.; Kamionka, E.; Desrousseaux, M. L.; Texier, H.; Gavalda, S.; et al. An engineered PET depolymerase to break down and recycle plastic bottles. *Nature* **2020**, *580* (7802), 216-219. DOI: 10.1038/s41586-020-2149-4.

(16) Branson, Y.; Soltl, S.; Buchmann, C.; Wei, R.; Schaffert, L.; Badenhorst, C. P. S.; Reisky, L.; Jager, G.; Bornscheuer, U. T. Urethanes for the Enzymatic Hydrolysis of Low Molecular Weight Carbamates and the Recycling of Polyurethanes. *Angew Chem Int Ed Engl* **2023**, *62* (9), e202216220. DOI: 10.1002/anie.202216220 From NLM Medline.

(17) Neu, D.; Lehmann, T.; Elleuche, S.; Pollmann, S. Arabidopsis amidase 1, a member of the amidase signature family. *The FEBS Journal* **2007**, *274* (13), 3440-3451. DOI: <https://doi.org/10.1111/j.1742-4658.2007.05876.x> (accessed 2024/06/26).

(18) Neumann, S.; Granzin, J.; Kula, M. R.; Labahn, J. Crystallization and preliminary X-ray data of the recombinant peptide amidase from *Stenotrophomonas maltophilia*. *Acta Crystallogr. D Biol. Crystallogr.* **2002**, *58* (Pt 2), 333-335. DOI: 10.1107/s0907444901020248 From NLM Medline.

(19) Shin, S.; Lee, T. H.; Ha, N. C.; Koo, H. M.; Kim, S. Y.; Lee, H. S.; Kim, Y. S.; Oh, B. H. Structure of malonamidase E2 reveals a novel Ser-cisSer-Lys catalytic triad in a new serine hydrolase fold that is prevalent in nature. *EMBO J.* **2002**, *21* (11), 2509-2516. DOI: 10.1093/emboj/21.11.2509 From NLM Medline.

- (20) Cerqueira, N. M. F. S. A.; Moorthy, H.; Fernandes, P. A.; Ramos, M. J. The mechanism of the Ser-(cis)Ser-Lys catalytic triad of peptide amidases. *Physical Chemistry Chemical Physics* **2017**, *19* (19), 12343-12354, 10.1039/C7CP00277G. DOI: 10.1039/C7CP00277G.
- (21) Olsson, M. H. M.; Søndergaard, C. R.; Rostkowski, M.; Jensen, J. H. PROPKA3: Consistent Treatment of Internal and Surface Residues in Empirical pKa Predictions. *J. Chem. Theory Comput.* **2011**, *7* (2), 525-537. DOI: 10.1021/ct100578z.
- (22) Dennington, R.; Keith, T.; Millam, J. GaussView, Version 5. *Semichem Inc., Shawnee Mission, KS* **2009**.
- (23) Frisch, M. J. T., G. W.; Schlegel, H. B.; Scuseria, G. E.; Robb, M. A.; Cheeseman, J. R.; Scalmani, G.; Barone, V.; Petersson, G. A.; Nakatsuji, H.; Li, X.; Caricato, M.; Marenich, A.; Bloino, J.; Janesko, B. G.; Gomperts, R.; Mennucci, B.; Hratchian, H. P.; Ortiz, J. V.; Izmaylov, A. F.; Sonnenberg, J. L.; Williams-Young, D.; Ding, F.; Lipparini, F.; Egidi, F.; Goings, J.; Peng, B.; Petrone, A.; Henderson, T.; Ranasinghe, D.; Zakrzewski, V. G.; Gao, J.; Rega, N.; Zheng, G.; Liang, W.; Hada, M.; Ehara, M.; Toyota, K.; Fukuda, R.; Hasegawa, J.; Ishida, M.; Nakajima, T.; Honda, Y.; Kitao, O.; Nakai, H.; Vreven, T.; Throssell, K.; Montgomery, Jr., J. A.; Peralta, J. E.; Ogliaro, F.; Bearpark, M.; Heyd, J. J.; Brothers, E.; Kudin, K. N.; Staroverov, V. N.; Keith, T.; Kobayashi, R.; Normand, J.; Raghavachari, K.; Rendell, A.; Burant, J. C.; Iyengar, S. S.; Tomasi, J.; Cossi, M.; Millam, J. M.; Klene, M.; Adamo, C.; Cammi, R.; Ochterski, J. W.; Martin, R. L.; Morokuma, K.; Farkas, O.; Foresman, J. B.; Fox, D. J. *Gaussian 09. Gaussian, Inc.: Wallingford, CT* **2009**.
- (24) Jones, G.; Willett, P.; Glen, R. C.; Leach, A. R.; Taylor, R. Development and validation of a genetic algorithm for flexible docking. *J. Mol. Biol.* **1997**, *267* (3), 727-748. DOI: 10.1006/jmbi.1996.0897.
- (25) Korb, O.; Stutzle, T.; Exner, T. E. Empirical scoring functions for advanced protein-ligand docking with PLANTS. *J. Chem. Inf. Model.* **2009**, *49* (1), 84-96. DOI: 10.1021/ci800298z
From NLM Medline.
- (26) Jorgensen, W. L.; Chandrasekhar, J.; Madura, J. D.; Impey, R. W.; Klein, M. L. Comparison of Simple Potential Functions for Simulating Liquid Water. *J. Chem. Phys.* **1983**, *79* (2), 926-935. DOI: Doi 10.1063/1.445869.
- (27) Case, D.; Ben-Shalom, I.; Brozell, S. R.; Cerutti, D. S.; Cheatham, T.; Cruzeiro, V. W. D.; Darden, T.; Duke, R.; Ghoreishi, D.; Gilson, M.; et al. *Amber 2018*; 2018.
- (28) Wang, J.; Wolf, R. M.; Caldwell, J. W.; Kollman, P. A.; Case, D. A. Development and testing of a general amber force field. *J. Comput. Chem.* **2004**, *25* (9), 1157-1174. DOI: 10.1002/jcc.20035.

- (29) Maier, J. A.; Martinez, C.; Kasavajhala, K.; Wickstrom, L.; Hauser, K. E.; Simmerling, C. ff14SB: Improving the Accuracy of Protein Side Chain and Backbone Parameters from ff99SB. *J. Chem. Theory Comput.* **2015**, *11* (8), 3696-3713. DOI: 10.1021/acs.jctc.5b00255 From NLM Medline.
- (30) Cornell, W. D.; Cieplak, P.; Bayly, C. I.; Kollman, P. A. Application of RESP charges to calculate conformational energies, hydrogen bond energies, and free energies of solvation. *Journal of the American Chemical Society* **1993**, *115* (21), 9620-9631. DOI: 10.1021/ja00074a030.
- (31) Abraham, M. J.; Murtola, T.; Schulz, R.; Páll, S.; Smith, J. C.; Hess, B.; Lindahl, E. GROMACS: High performance molecular simulations through multi-level parallelism from laptops to supercomputers. *SoftwareX* **2015**, *1-2*, 19-25. DOI: <https://doi.org/10.1016/j.softx.2015.06.001>.
- (32) Van Der Spoel, D.; Lindahl, E.; Hess, B.; Groenhof, G.; Mark, A. E.; Berendsen, H. J. GROMACS: fast, flexible, and free. *J. Comput. Chem.* **2005**, *26* (16), 1701-1718. DOI: 10.1002/jcc.20291 From NLM Medline.
- (33) Cauchy, A. Méthode générale pour la résolution des systemes d'équations simultanées. *Comp. Rend. Sci. Paris* **1847**, *25* (1847), 536-538.
- (34) Hess, B.; Bekker, H.; Berendsen, H. J. C.; Fraaije, J. G. E. M. LINCS: A linear constraint solver for molecular simulations. *J. Comput. Chem.* **1997**, *18* (12), 1463-1472, [https://doi.org/10.1002/\(SICI\)1096-987X\(199709\)18:12<1463::AID-JCC4>3.0.CO;2-H](https://doi.org/10.1002/(SICI)1096-987X(199709)18:12<1463::AID-JCC4>3.0.CO;2-H). DOI: [https://doi.org/10.1002/\(SICI\)1096-987X\(199709\)18:12<1463::AID-JCC4>3.0.CO;2-H](https://doi.org/10.1002/(SICI)1096-987X(199709)18:12<1463::AID-JCC4>3.0.CO;2-H) (accessed 2023/06/26).
- (35) Essmann, U.; Perera, L.; Berkowitz, M. L.; Darden, T.; Lee, H.; Pedersen, L. G. A smooth particle mesh Ewald method. *The Journal of Chemical Physics* **1995**, *103* (19), 8577-8593. DOI: 10.1063/1.470117 (accessed 6/26/2023).
- (36) Bussi, G.; Donadio, D.; Parrinello, M. Canonical sampling through velocity rescaling. *J. Chem. Phys.* **2007**, *126* (1), 014101. DOI: 10.1063/1.2408420 From NLM PubMed-not-MEDLINE.
- (37) Berendsen, H. J. C.; Postma, J. P. M.; van Gunsteren, W. F.; DiNola, A.; Haak, J. R. Molecular dynamics with coupling to an external bath. *The Journal of Chemical Physics* **1984**, *81* (8), 3684-3690. DOI: 10.1063/1.448118 (accessed 6/26/2023).
- (38) Parrinello, M.; Rahman, A. Polymorphic transitions in single crystals: A new molecular dynamics method. *J. Appl. Phys.* **1981**, *52* (12), 7182-7190. DOI: 10.1063/1.328693 (accessed 6/26/2023).

- (39) Svensson, M.; Humbel, S.; Froese, R. D. J.; Matsubara, T.; Sieber, S.; Morokuma, K. ONIOM: A multilayered integrated MO+MM method for geometry optimizations and single point energy predictions. A test for Diels-Alder reactions and Pt(P(t-Bu)(3))(2)+H-2 oxidative addition. *J. Phys. Chem.* **1996**, *100* (50), 19357-19363. DOI: DOI 10.1021/jp962071j.
- (40) Das, D.; Eurenus, K. P.; Billings, E. M.; Sherwood, P.; Chatfield, D. C.; Hodošček, M.; Brooks, B. R. Optimization of quantum mechanical molecular mechanical partitioning schemes: Gaussian delocalization of molecular mechanical charges and the double link atom method. *The Journal of Chemical Physics* **2002**, *117* (23), 10534-10547. DOI: 10.1063/1.1520134 (accessed 6/27/2024).
- (41) Singh, U. C.; Kollman, P. A. A combined ab initio quantum mechanical and molecular mechanical method for carrying out simulations on complex molecular systems: Applications to the CH₃Cl + Cl⁻ exchange reaction and gas phase protonation of polyethers. *J. Comput. Chem.* **1986**, *7* (6), 718-730. DOI: <https://doi.org/10.1002/jcc.540070604> (accessed 2024/06/27).
- (42) Humphrey, W.; Dalke, A.; Schulten, K. VMD: visual molecular dynamics. *J. Mol. Graph.* **1996**, *14* (1), 33-38, 27-38. DOI: 10.1016/0263-7855(96)00018-5 From NLM Medline.
- (43) S. Fernandes, H.; Ramos, M. J.; M. F. S. A. Cerqueira, N. molUP: A VMD plugin to handle QM and ONIOM calculations using the gaussian software. *J. Comput. Chem.* **2018**, *39* (19), 1344-1353. DOI: 10.1002/jcc.25189 (accessed 2018/12/04).
- (44) Becke, A. D. Density-functional exchange-energy approximation with correct asymptotic behavior. *Physical Review A* **1988**, *38* (6), 3098-3100. DOI: 10.1103/PhysRevA.38.3098.
- (45) Lee, C.; Yang, W.; Parr, R. G. Development of the Colle-Salvetti correlation-energy formula into a functional of the electron density. *Physical Review B* **1988**, *37* (2), 785-789. DOI: 10.1103/PhysRevB.37.785.
- (46) Grimme, S.; Ehrlich, S.; Goerigk, L. Effect of the damping function in dispersion corrected density functional theory. *J. Comput. Chem.* **2011**, *32* (7), 1456-1465. DOI: 10.1002/jcc.21759 (accessed 2020/01/31).
- (47) Neves, R. P. P.; Fernandes, P. A.; Ramos, M. J. Mechanistic insights on the reduction of glutathione disulfide by protein disulfide isomerase. *Proc. Natl. Acad. Sci. U. S. A.* **2017**, *114* (24), E4724-E4733. DOI: 10.1073/pnas.1618985114.
- (48) Neese, F. Software update: the ORCA program system, version 4.0. *Wiley Interdiscip Rev Comput Mol Sci* **2018**, *8*:e1327 (1), DOI: 10.1002/wcms.1327. DOI: 10.1002/wcms.1327.

- (49) McKinney, M. K.; Cravatt, B. F. Structure and function of fatty acid amide hydrolase. *Annu Rev Biochem* **2005**, *74*, 411-432. DOI: 10.1146/annurev.biochem.74.082803.133450 From NLM Medline.
- (50) Sousa, S. F.; Calixto, A. R.; Ferreira, P.; Ramos, M. J.; Lim, C.; Fernandes, P. A. Activation Free Energy, Substrate Binding Free Energy, and Enzyme Efficiency Fall in a Very Narrow Range of Values for Most Enzymes. *ACS Catal.* **2020**, *10* (15), 8444-8453. DOI: 10.1021/acscatal.0c01947.
- (51) Remko, M.; Rode, B. M. Ab initio study of decomposition of carbamic acid and its thio and sila derivatives. *Journal of Molecular Structure: THEOCHEM* **1995**, *339* (1), 125-131. DOI: [https://doi.org/10.1016/0166-1280\(95\)04158-3](https://doi.org/10.1016/0166-1280(95)04158-3).
- (52) Ouellette, R. J.; Rawn, J. D. 15 - Synthetic Polymers. In *Principles of Organic Chemistry*, Ouellette, R. J., Rawn, J. D. Eds.; Elsevier, 2015; pp 397-419.
- (53) Bayer, T.; Palm, G. J.; Berndt, L.; Meinert, H.; Branson, Y.; Schmidt, L.; Cziegler, C.; Somvilla, I.; Zurr, C.; Graf, L. G.; et al. Structural Elucidation of a Metagenomic Urethanase and Its Engineering Towards Enhanced Hydrolysis Profiles. *Angew Chem Int Ed Engl* **2024**, e202404492. DOI: 10.1002/anie.202404492 From NLM Publisher.
- (54) Medina, F. E.; Neves, R. P. P.; Ramos, M. J.; Fernandes, P. A. QM/MM Study of the Reaction Mechanism of the Dehydratase Domain from Mammalian Fatty Acid Synthase. *ACS Catal.* **2018**, *8* (11), 10267-10278. DOI: 10.1021/acscatal.8b02616.
- (55) Ribeiro, A. J. M.; Santos-Martins, D.; Russo, N.; Ramos, M. J.; Fernandes, P. A. Enzymatic Flexibility and Reaction Rate: A QM/MM Study of HIV-1 Protease. *ACS Catal.* **2015**, *5* (9), 5617-5626. DOI: 10.1021/acscatal.5b00759.
- (56) Sousa, J. P. M.; Neves, R. P. P.; Sousa, S. F.; Ramos, M. J.; Fernandes, P. A. Reaction Mechanism and Determinants for Efficient Catalysis by DszB, a Key Enzyme for Crude Oil Bio-desulfurization. *ACS Catal.* **2020**, *10* (16), 9545-9554. DOI: 10.1021/acscatal.0c03122.

For Table of Contents Only

